

OPEN

Terahertz Magneto-Optic Sensor/Imager

Dmitry S. Bulgarevich^{1,2*}, Yusuke Akamine², Miezel Talara², Valynn Mag-usara², Hideaki Kitahara², Hiroyuki Kato², Masaki Shiihara², Masahiko Tani² & Makoto Watanabe¹

We are reporting a new type of compact magneto-optic sensor constructed from terahertz-wave spintronic emitter and electro-optic detector. The corresponding terahertz polarization output of the emitter and the detection phase-sensitivity of the detector depend on the vector of the external magnetic field. The emitter/detector pair consists of two small and thin wafers sandwiched together and capped with a thin gold mirror. As a result, the use of bulky terahertz steering/collection optics was completely eliminated in our magneto-optic imager. With such simple on-chip generation/detection scheme for terahertz time-domain setup in reflection-type geometry, we were able to record the raster-scanned image contrast of a permanent magnet in the proximity of the sensor surface. The contrast strongly varies with the magnet orientation and its position with respect to the sensor. The imager spatial resolution depends on chip optical quality for tight femtosecond-laser pump/probe cross-focusing at detector/mirror interface and terahertz generation/detection efficiency. In this respect, the chip robustness to the pump/probe fluences is also an important factor to consider.

The main advantage of typical magneto-optic imager/imaging (MOI)^{1–7} over magnetic field imager/imaging (MFI) is the possibility of achieving higher spatial resolution by using visible light sources and smaller sizes of the sensing domains. The highest reported spatial resolutions with MOI by using large-area Faraday rotator sensors were between 0.5 and 100 μm , which were limited by the magnetic domain periodicity and thickness of the sensor layer^{8–10}. A maximum of 10- μT magnetic field resolution/sensitivity with MOI was observed⁸. Although magneto-optical Kerr effect microscopy (MOKE) can also provide up to 0.2- μm spatial resolution, it is limited to materials with strong Kerr response¹¹. The μT range magnetic sensitivity of nitrogen-vacancy centres in diamond can also be used for imaging of stray magnetic fields in thin ferromagnetic films with 0.44- μm spatial resolution¹².

On the other hand, the MFI with superconducting quantum interference device (SQUID), giant magnetoresistance (GMR), anisotropic magnetoresistance (AMR), extraordinary magnetoresistance (EMR), giant magneto-impedance (GMI), tunnel magnetoresistance (TMR), Hall effect, microelectromechanical systems (MEMS), etc. sensors can also offer excellent magnetic field sensitivity/resolution up to aT range, but with reduced spatial resolution (worse than 100 μm).

In this respect, the development of new type MOIs for non-destructive testing (NDT) applications with detection of magnetic flux leakage (MFL) above the sample surface is still an important topic in terms of finding the balance between MOI spatial and axial resolutions, magnetic field sensitivity, physical size, robustness, operation conditions, cost, applications, etc. factors. In this work, we describe our first attempt to develop the novel MOI based on recently reported spintronic terahertz (THz) emitters^{13–15} and well-known electro-optic (EO) THz detectors¹⁶ for THz time-domain spectroscopy (TDS)^{17,18}. The magnetic field is the key factor for generation of spintronic THz emission and there are several recent reports on magnetic-field tailoring of the terahertz polarization and amplitude^{19–21}. The possibility of external magnetic field distribution mapping using terahertz emission from semiconductor surfaces was also demonstrated²². Although, the THz MOI was not reported yet.

Experimental

Figure 1 shows the schematics of the reflection-type THz-TDS imaging setup (avpIRS-500-SP, Aispec Instruments) we used with some modifications to accommodate the EO sampling and achieve tight refocusing for THz generation/detection with our MOI chip²³. Figure 2 depicts the side view of the MOI chip assembly and the spintronic emitter structure as well as the magnified image of the focusing optics, chip rotation holder, and scanning sample holder with attached permanent magnet. The ~ 10 -fs pump/probe beams ($\lambda = 780$ nm

¹Research Center for Structural Materials, National Institute for Materials Science, 1-2-1 Sengen, Tsukuba, Ibaraki, 305-0047, Japan. ²Research Center for Development of Far-Infrared Region, University of Fukui, Fukui, 3-9-1 Bunkyo, 910-8507, Japan. *email: BULGAREVICH.Dmitry@nims.go.jp

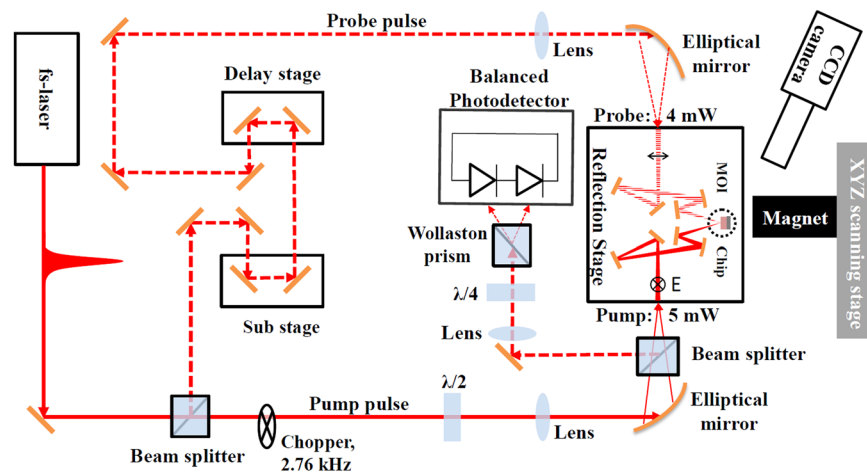


Figure 1. The schematic of the reflection-type THz-TDS MOI setup with EO sampling.

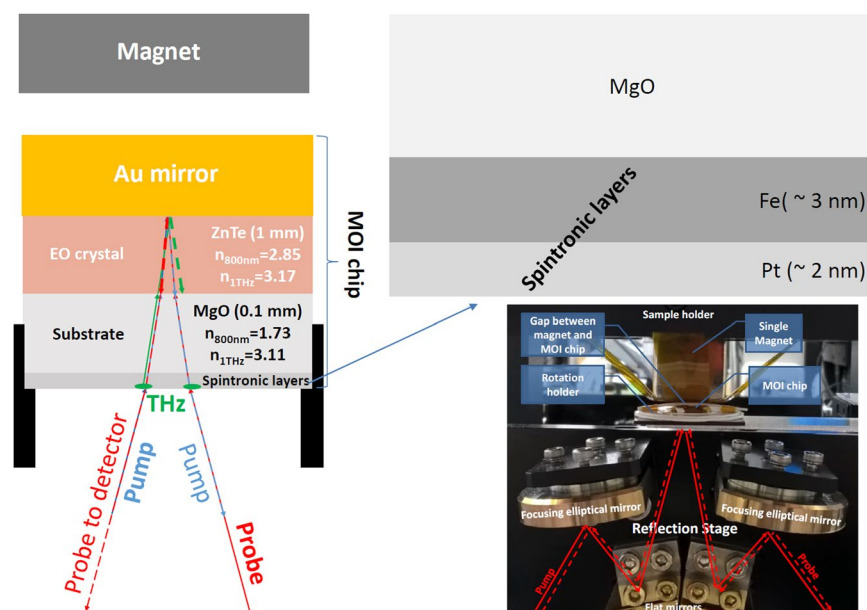


Figure 2. The schematic drawings of the on-chip sensor for THz-TDS MOI, the structure of the THz wave spintronic emitter, and close-up photo with focusing optics, sensor rotation holder, and permanent magnet on XYZ-scanning stage holder.

central wavelength, 80 MHz repetition rate, 5/4 mW power) emitted from the Integral Element PRO 400 (Spectra-Physics) laser source are incident to the reflection stage with refocusing/steering optics from opposite directions and are cross-focused at the ZnTe/Au-mirror interface. Since good cross-focusing is crucial for THz signal detection, the design allows for the Au-mirror to be removable when a CCD camera with long working distance objective is used for initial alignments/focusing at ZnTe/air interface.

As shown in Fig. 2, the pump beam hits the MOI chip from the spintronic layer side and generates the electron currents in vertical direction within the thin metallic films. If the ferromagnetic (FM) Fe layer is magnetized, the mobility of the majority spin-up electrons is higher compared to that of the minority spin-down electrons. In the non-magnetic (NM) Pt layer with strong spin-orbit interaction, the spin-up and spin-down electrons deflect in opposite directions and produce the ultrafast transverse charge current by inverse spin-Hall effect²⁴ (ISHE). This current is the source of the THz radiation from the spintronic layer¹³. The linear polarization of such THz emission is orthogonal to the magnetization vector, it can be modulated/changed even by relatively weak magnetic field (below 10 mT), and it is independent on pump polarization.

Then, THz radiation from the spintronic layer propagates through the MgO substrate and EO ZnTe wafers, reflects from the Au-mirror, and co-propagates inside the ZnTe wafer with the probe beam reflected from the Au-mirror. The divergence angle between the THz/probe fronts (see bold green and red dashed arrows in Fig. 2) is $\sim 15^\circ$ with our re-focusing optics. At this stage, the probe beam linear polarization is perturbed by the THz

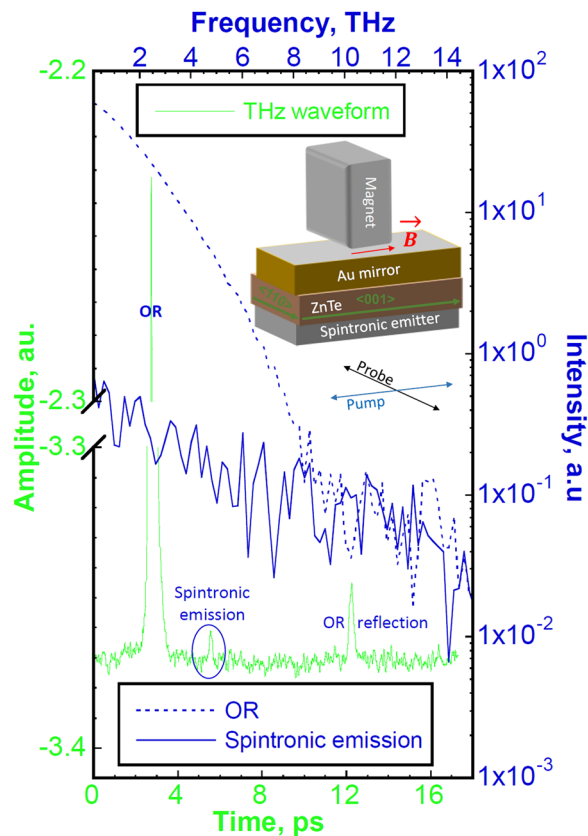


Figure 3. The THz waveform collected with displayed optical setup of MOI chip, permanent magnet, and pump/probe polarizations. The scale colours correspond to the plot ones. For OR and spintronic emissions in frequency domains, the 0–5 and 5–10 ps waveform portions were used in FFT calculations, respectively.

electric field in the EO crystal. Finally, the induced ellipticity component of probe polarization is analysed with standard EO-sampling assembly in the THz-TDS setup, which results in the recording of THz waveforms or/and images. Note that initial pump/probe linear polarizations were orthogonal to each other and in-plane with the spintronic layer/air interface. The MOI chip was also aligned in a calibrated rotation holder to have the pump beam polarization orthogonal to the $\langle 110 \rangle$ axis of ZnTe crystal in order to suppress the parasitic THz emission generated inside the EO crystal by optical rectification (OR) due to moderate ~ 0.2 mJ/cm² pump/probe fluences with our cross-focusing setup.

In this work, we utilized the previously optimized Fe/Pt spintronic bilayer structure for maximum THz emission output¹⁴. It consists of 2-nm Fe and 3-nm Pt layers (see Fig. 2), which can be grown by molecular beam epitaxy or electron beam evaporation on 500- μ m MgO substrate (Tateho Chemical Industries Co., Ltd.). The both side polished ZnTe (110) crystal with $11 \times 9 \times 1$ mm³ dimensions (Techno Chemicals, Inc.) was used for EO detection.

The magnetic field properties of used permanent magnet were visualized and characterized with Magnetic Field Visualize Sheet (C-Task Un-Digital) and Gauss Meter with Hall sensor (Model 410, Lake Shore Cryotronics, Inc), respectively. The image post-processing was done with FIJI software package²⁵.

Results and discussion

Figure 3 shows the typical unipolar waveform collected by using the indicated magneto-optical setup. One of the advantages of using an on-chip THz generation/detection scheme is that the atmospheric water vapour does not influence the measured signals. For this on-chip THz generation/detection scheme, the main THz peak is insensitive to the magnet position and originates from the parasitic OR of the pump beam in the ZnTe crystal. The weakest signal is delayed from such OR at $\sim +2.8$ ps after propagation to ZnTe/Au interface. Such delay is due to the difference in refractive indexes for optical pump and spintronic-emitter-generated THz fronts in MgO and ZnTe wafers (see Fig. 2). This signal is well separated from the OR peak to get any parasitic effect on the MOI measurements. At constant pump/probe powers, its peak amplitude and phase are affected only by the strength and vector of the external magnetic field (discussed below). After magnet removal, this signal could be registered for days before complete disappearance due to slow de-magnetization of the Fe layer.

The moderate waveform peak at $\sim +9.5$ ps is due to the reflection of the OR-generated THz front at the ZnTe/MgO interface and partial co-propagation in ZnTe with the incoming probe beam (see Fig. 2). As such, this waveform peak is also insensitive to the magnetic field. With currently available pump/probe powers in our MOI setup, the signal-to noise ratio (SNR ≤ 1) is low for spintronic emission, so multiple waveform or signal averaging

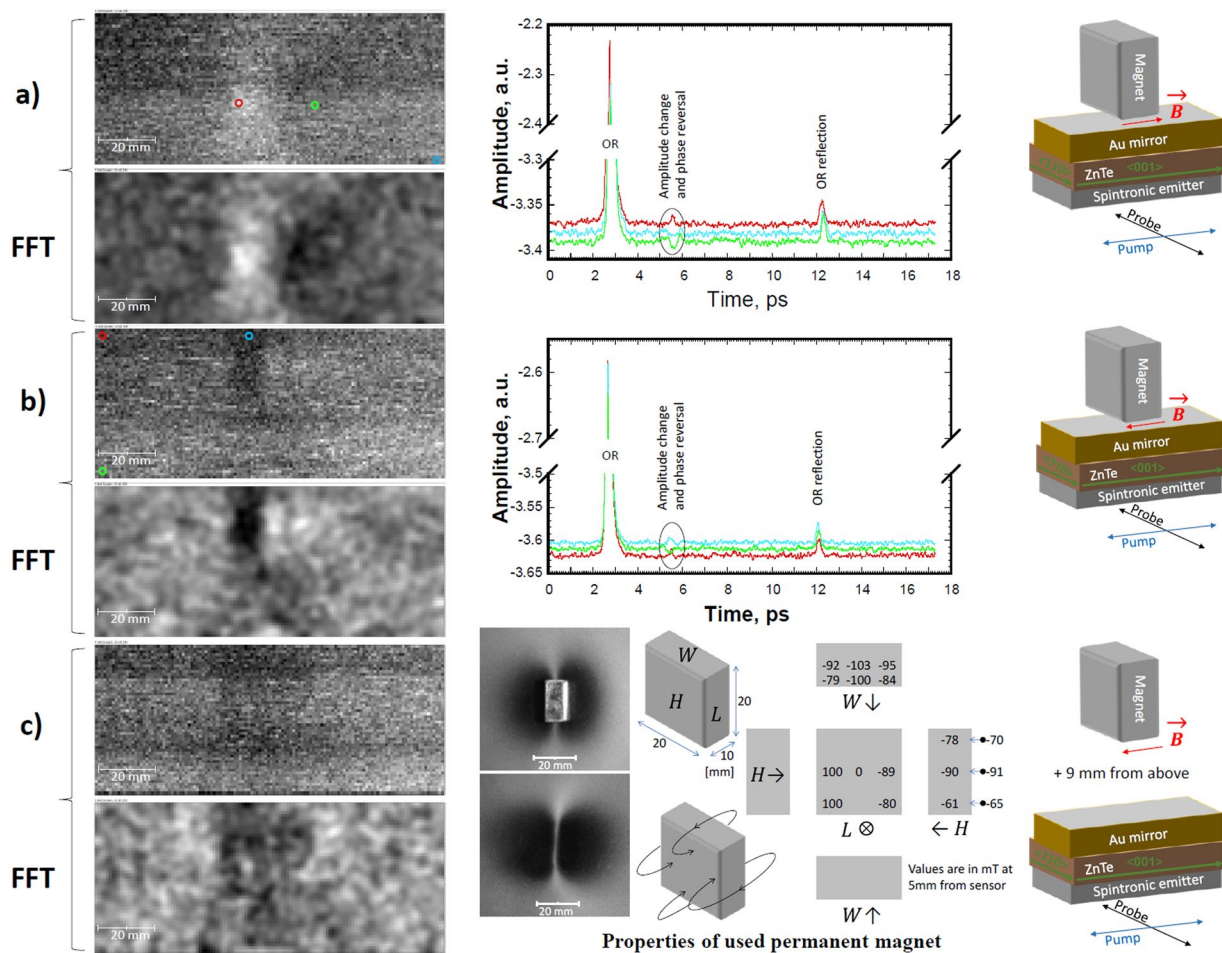


Figure 4. MOI results with different permanent magnet orientation with respect to the on-chip THz sensor (see text for more details). The magnet in (a) and (b) was ~5 mm above the spintronic layer surface. The waveform colours correspond to ones of the circles that indicate the spatial positions on images for their collections. The photos of used magnet positioned above and below of the MFVS are in (c) together with other drawings and data for magnet properties.

was used to improve it. With 32 times averaging, the $SNR = A_{signal}/RMS_{noise} \cong 4$, where A_{signal} is the amplitude of the magnetic field sensitive signal and RMS_{noise} is the root mean square of the noise amplitude (see Fig. 3 for THz waveform). By using the fast Fourier transform (FFT) on collected waveform, the response in frequency domain for OR and spintronic emissions are also shown for comparison in Fig. 3. With 32 times averaging, the spintronic emission bandwidth is ~4–5 THz.

Figures 4(a–c) and 5(a–c) show the images for indicated magnetic field vector (B) directions in the magnet/MOI-chip setup and oscillating electric field vectors/polarizations (E) of pump/probe beams. They were collected at fixed delay stage position, which corresponded to the magnetic-field-sensitive waveform maximum at ~+2.8 ps from the OR peak maximum. During continuous ~0.5 s/pixel X-scanning stage movement with attached magnet, the waveform amplitude at this delay stage position was sampled 16 times for averaging within each 1×1 mm pixel. It took ~1 h for the collection of each original image shown in Figs. 4 and 5. To improve the image contrast, bandpass filtering with FFT was applied. As shown in Figs. 4 and 5, filtering suppresses the horizontal stripes generated by some THz-TDS system instability. It also smoothens the variations of each image's bright and dark patches with sizes larger than 40 pixels and strongly attenuates the objects smaller than 3 pixels²⁶.

The 32 time-averaged waveforms collected at different spatial positions are also shown in Figs. 4 and 5. These waveforms demonstrate that the signal for magnetic-field-sensitive peak can change not only its intensity depending on MOI-chip vs magnet position/orientation, but also its phase. This explains the image contrast reversal depending on the direction of the magnetic field vector (compare Fig. 4(a,b) as well as Fig. 5(a,b)).

If α is the angle of the THz beam polarization with respect to the (110) axis of ZnTe crystal, then the EO sampling signal will depend on it by a factor of $\sqrt{1 + 3\cos^2\alpha}$. It should be noted that the polarization of THz emission from the spintronic layer is always orthogonal to the component of the B vector oriented in-plane with our MOI sensor surface. This in-plane B vector component changes with the magnet position and orientation with respect to the pump beam spot on the MOI sensor during imaging due to the re-magnetization of the spintronic layer at this spot. As a result, the EO sampling detects amplitude and phase variations in the THz signal effected by such

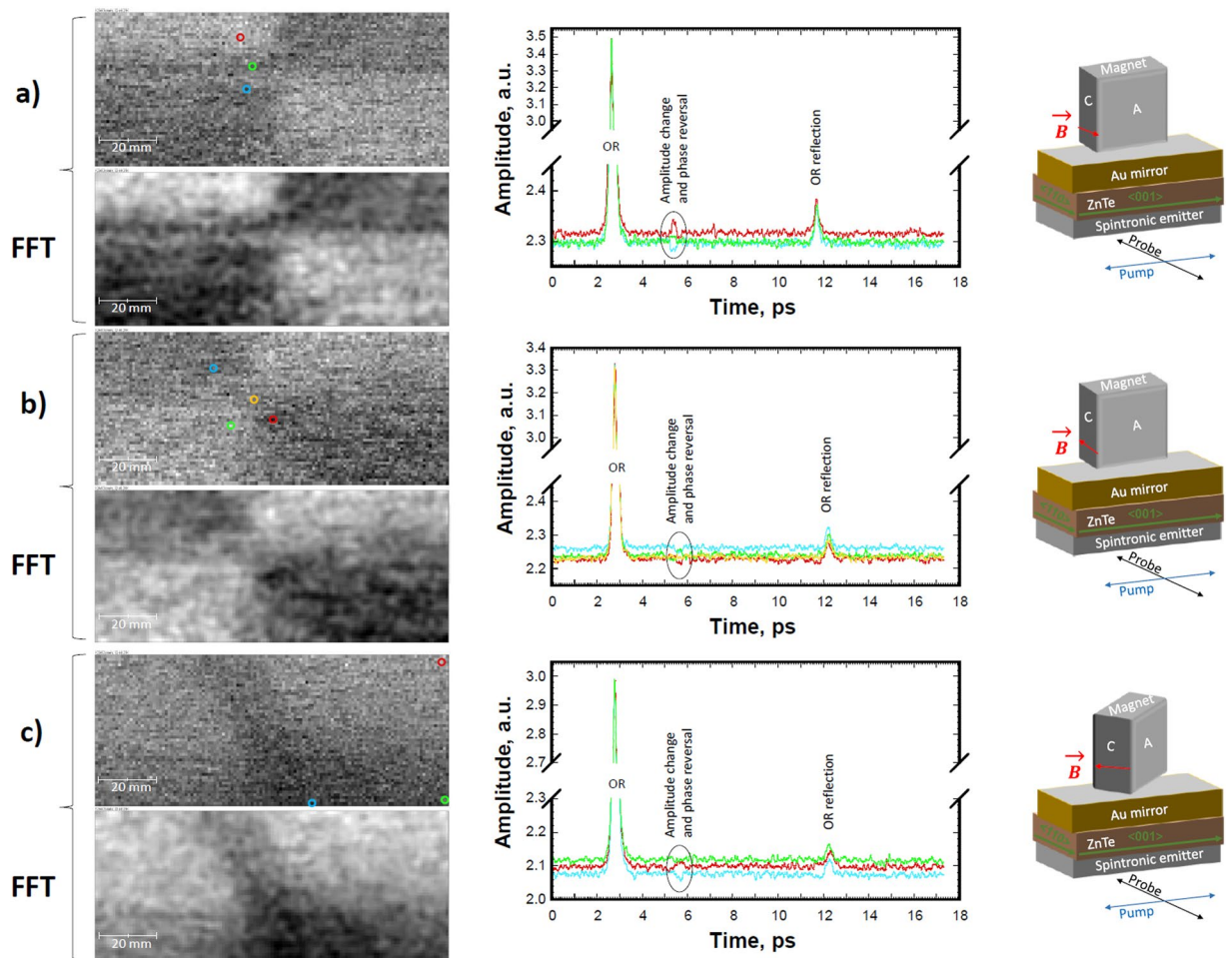


Figure 5. MOI results with different permanent magnet orientation with respect to the on-chip THz sensor. The magnet in (a), (b), and (c) was ~ 5 mm above the spintronic layer surface. The waveform colours correspond to ones of the circles, which indicate the spatial positions on images for their collections.

re-magnetization, which leads to the possibility of MOI with our sensor chip. In other words, our MOI constantly detects the current magnetization state within the spot of the focused pump beam on the spintronic layer. The resulted MOI is a convolution of spintronic emitter efficiency and EO detector sensitivity to spintronic layer magnetization.

Comparing of THz MOI images with photos of Magnetic Field Visualize Sheet (MFVS) in Fig. 4, it can be seen that THz MOI gives better magnet shape visualization. So far however, the THz MOI has lower sensitivity/resolution to the magnetic field. Note that in Fig. 4 (c) with photos of permanent magnet on top and under of the MFVS, the bright and dark areas indicate the predominance of in-plane and out-of-plane components of the magnetic field lines with respect to the plane of the MFVS surface, respectively. Such magnetic field induced contrast is due to the different reflectivity of aligned nickel flakes (parallel or edge-on to the MFVS surface) suspended in oil micro-capsules between flexible translucent and substrate thin sheets. For areas far away from magnet (not shown), the image contrast indicates the magnetization state history of MFVS unrelated to the current magnet position in Fig. 4 (c). Therefore, our THz MOI demonstrates the consistent results with MFVS.

In principle, the lateral spatial resolution of our MOI should be governed by the optical resolution of the pump/probe focusing optics. The axial resolution depends on the magnetic field sensitivity with EO sampling and can affect the spatial one. This was the case with our current THz-TDS setup. The lateral resolution was low due to poor image contrast brought by a low magnetic field sensitivity. To improve the SNR, a higher pump power is needed. In the current set-up, we used a 5mW (~ 0.2 mJ/cm² fluence) pump power. Previous study reported that this spintronic layer could withstand up to ~ 25 times higher fluence¹⁴. However, the linear relation was observed between pump power and THz output amplitude (slope is ~ 1) only up to ~ 0.25 mJ/cm² fluence¹⁵. Nevertheless, the EO SNR is expected to be improved at higher fluences. For example, it was reported that in nonlinear regime from ~ 0.25 to ~ 1.25 mJ/cm², the THz signal amplitude increased ~ 2 times²⁷. Note that 1.25 mJ/cm² fluence is still ~ 5 times lower than our spintronic layer damage threshold.

In addition, we expect that by modifying the spintronic layer structure into the antenna shape, the THz output amplitude and beam directivity could improve the EO signal at least 8 times²⁸. Further investigations on spintronic layer materials with large spin Hall angle²⁹, layer thickness, and layer sequence could lead to additional improvements. The spintronic layer composition also could be optimized to have the wider/smoother

dependence of THz emission amplitude on magnetic field strength²¹. Recently, the sub-mT sensitivity of THz emission was reported with Co₂₀Fe₆₀B₂₀/Pt spintronic bilayer³⁰.

Moreover, the optical losses could be decreased by eliminating the use of MgO and glass substrates and directly microfabricating the spintronic and mirror layers on EO-detector chip surface. Besides EO sampling, the development of suitable on-chip photoconductive antenna or spintronic detector is another way to improve the THz MOI sensitivity. It is also expected that magnetic field modulation will increase the SNR. As for image collection speed, the use of higher pump/probe modulation rate could also enhance the image scanning velocity. In summary, we expect that SNR with our MOI could be improved with additional studies/modifications.

Concluding remarks

To our best knowledge, we are reporting the first MOI with on-chip emitter/detector sensor for THz-TDS. By improving its SNR, this technique could significantly contribute to the very limited number of reported MOI schemes for NDT applications. Potentially, our scheme has an advantage over Faraday-based and Kerr effect-based techniques in terms of likely achievable spatial resolution and applicability to various materials.

Received: 12 November 2019; Accepted: 8 January 2020;

Published online: 24 January 2020

References

1. Diraison, Y. L., Joubert, P.-Y. & Placko, D. Characterization of subsurface defects in aeronautical riveted lap-joints using multi-frequency eddy current imaging. *NDT&E Int.* **42**, 133–140 (2009).
2. Deng, Y. & Liu, X. Electromagnetic imaging methods for nondestructive evaluation applications. *Sensors* **11**, 11774–11808 (2011).
3. Cheng, Y., Deng, Y., Bai, L. & Chen, K. Enhanced laser-based magneto-optic imaging system for nondestructive evaluation applications. *IEEE Trans. Instrum. Meas.* **62**, 1192–1198 (2013).
4. Novotný, P., Sajdl, P. & Macháč, P. A magneto-optic imager for NDT applications. *NDT&E Int.* **37**, 645–649 (2004).
5. Deng, Y. *et al.* Characterization of magneto-optic imaging data for aircraft inspection. *IEEE Trans. Magn.* **42**, 3228–3230 (2006).
6. Cheng, Y. H., Zhou, Z. F. & Tian, G. Y. Enhanced magneto-optic imaging system for nondestructive evaluation. *NDT&E Int.* **40**, 374–377 (2007).
7. Tehranchia, M. M., Hamidi, S. M., Eftekhari, H., Karbaschi, M. & Ranjbaran, M. The inspection of magnetic flux leakage from metal surface cracks by magneto-optical sensors. *Sens. Actuator A-Phys.* **172**, 365–368 (2011).
8. Koblishka, M. R. & Wijngaarden, R. J. Magneto-optical investigations of superconductors. *Supercond. Sci. Technol.* **8**, 199–213 (1995).
9. Nistor, I., Holthaus, C., Mayergoyz, I. D. & Kraff, C. Nonscanning imaging of two-dimensional magnetic patterns with submicron resolution using thin garnet films. *IEEE Trans. Magn.* **42**, 3255–3257 (2006).
10. Joubert, P.-Y. & Pinassaud, J. Linear magneto-optic imager for non-destructive evaluation. *Sens. Actuator A-Phys.* **129**, 126–130 (2006).
11. Urs, N. O. *et al.* Advanced magneto-optical microscopy: Imaging from picoseconds to centimeters - imaging spin waves and temperature distributions. *AIP Adv.* **6**, 055605–1–13 (2016).
12. Simpson, D. A. *et al.* Magneto-optical imaging of thin magnetic films using spins in diamond. *Sci. Rep.* **6**, 22797–1–8 (2016).
13. Seifert, T. S. *et al.* Efficient metallic spintronic emitters of ultrabroadband terahertz radiation. *Nat. Photonics* **10**, 483–488 (2016).
14. Torosyan, G., Keller, S., Scheuer, L., Beigang, R. & Papaioannou, E. T. Optimized spintronic terahertz emitters based on epitaxial grown Fe/Pt layer structures. *Sci. Rep.* **8**, 1311–1–9 (2018).
15. Papaioannou, E. T. *et al.* Efficient terahertz generation using Fe/Pt spintronic emitters pumped at different wavelengths. *IEEE Trans. Magn.* **54**, 9100205–1–5 (2018).
16. Gallot, G. & Grischkowsky, D. Electro-optic detection of terahertz radiation. *J. Opt. Soc. Am. B* **16**, 1204–1212 (1999).
17. Fattinger, C. & Grischkowsky, D. Terahertz beams. *Appl. Phys. Lett.* **54**, 490–492 (1989).
18. Dragomana, D. & Dragoman, M. Terahertz fields and applications. *Prog. Quant. Electron.* **28**, 1–66 (2004).
19. Hibberd, M. T. *et al.* Magnetic-field tailoring of the terahertz polarization emitted from a spintronic source. *Appl. Phys. Lett.* **114**, 031101–1–5 (2019).
20. Adam, R. *et al.* Magnetically and optically tunable terahertz radiation from Ta/NiFe/Pt spintronic nanolayers generated by femtosecond laser pulses. *Appl. Phys. Lett.* **114**, 212405–1–5 (2019).
21. Schneider, R. *et al.* Magnetic-field-dependent THz emission of spintronic TbFe/Pt layers. *ACS Photonics* **5**, 3936–3942 (2018).
22. Mag-usara, V. K., Bulgarevich, D. S., Shiwa, M., Watanabe, M. & Tani, M. External magnetic field distribution mapping using terahertz emission from indium antimonide. *Jpn. J. Appl. Phys.* **56**, 028001–1–3 (2017).
23. Bulgarevich, D. S., Watanabe, M. & Tani, M. Japan Patent Pending 2019-188010 (2019).
24. Saitoh, E., Ueda, M., Miyajima, H. & Tataru, G. Conversion of spin current into charge current at room temperature: inverse spin-Hall effect. *Appl. Phys. Lett.* **88**, 182509–1–3 (2006).
25. Schindelin, J. *et al.* Fiji: an open-source platform for biological-image analysis. *Nat. Methods* **9**, 676–682 (2012).
26. Ferreira, T. & Rasband, W. *ImageJ user guide IJ 1.46r* <http://imagej.nih.gov/ij/docs/guide> (2012).
27. Mag-usara, V. K. *et al.* Properties of an optimized Fe/Pt-based spintronic terahertz emitter: excitation power and wavelength dependences. *43rd International Conference on Infrared, Millimeter, and Terahertz Waves (IRMMW-THz)*, Japan, September 9–14 (2018).
28. Talara, M. *et al.* Efficient THz generation of diabolo-shaped spintronic Fe/Pt bilayer on MgO substrate using 780-nm Pump Wavelength. *The 80th JSAP Autumn Meeting*, Hokkaido, Japan, September 18–21 (2019).
29. Demasius, K. *et al.* Enhanced spin-orbit torques by oxygen incorporation in tungsten films. *Nat. Commun.* **7**, 10644 (2016).
30. Shorrock, A., Hibberd, M. T., Thomson, T., Nutter, P. W. & Graham, D. M. Role of magnetic field in THz emission from a spintronic source. *44rd International Conference on Infrared, Millimeter, and Terahertz Waves (IRMMW-THz)*, France, September 1–6 (2019).

Acknowledgements

This work was partially supported by NIMS Collaboration Research Grants: H29-68, H30-110, and 2019-105. We would like to thank Ohi Akihiko and Tomoko Ohki from NIMS Namiki Foundry as well as Katsuhiko Saito and Qixin Guo from Saga University for the microfabrication of spintronic structures.

Author contributions

D.S.B. wrote the manuscript and developed with M.T. the basic concept of MOI with on-chip THz sensor. Y.A., H.K., and V.M. designed/modified the THz-TDS optical setups and performed the MOI experiments with D.S.B., M.S., Hi.Ka., and Mi.Ta. V.M. and Mi.Ta. tested the performance of spintronic emitters for MOI chip. M.W. supervised this research and edited the manuscript. The manuscript was written up through contributions of all authors. All authors have given approval to the final version of the manuscript.

Competing interests

The authors declare no competing interests.

Additional information

Correspondence and requests for materials should be addressed to D.S.B.

Reprints and permissions information is available at www.nature.com/reprints.

Publisher's note Springer Nature remains neutral with regard to jurisdictional claims in published maps and institutional affiliations.



Open Access This article is licensed under a Creative Commons Attribution 4.0 International License, which permits use, sharing, adaptation, distribution and reproduction in any medium or format, as long as you give appropriate credit to the original author(s) and the source, provide a link to the Creative Commons license, and indicate if changes were made. The images or other third party material in this article are included in the article's Creative Commons license, unless indicated otherwise in a credit line to the material. If material is not included in the article's Creative Commons license and your intended use is not permitted by statutory regulation or exceeds the permitted use, you will need to obtain permission directly from the copyright holder. To view a copy of this license, visit <http://creativecommons.org/licenses/by/4.0/>.

© The Author(s) 2020